Probabilistic analysis of fracture reactivation associated with deep underground CO_2 injection

Jaewon Lee[1], Ki-Bok Min[1], Jonny Rutqvist[2]

[1] *Department of Energy Systems Engineering, Seoul National University, Seoul, South Korea*

[2] *Earth Sciences Division, Lawrence Berkeley National Laboratory, Berkeley, U.S.A.*

Abstract

In the context of carbon capture and storage, deep underground injection of CO_2 induces the geomechanical changes within and around the injection zone and their impact on CO_2 storage security should be evaluated. In this study, we conduct coupled multiphase fluid flow and geomechanical modeling to investigate such geomechanical changes, focusing on probabilistic analysis of injection induced fracture reactivation (such as shear slip) that could lead to enhanced permeability and CO_2 migration across otherwise low-permeability caprock formations. Fracture reactivation in terms of shear slip was analyzed by implicitly considering the fracture orientations generated using the Latin hypercube sampling method, in one case using published fracture statistics from a CO_2 storage site. The analysis was conducted by a coupled multiphase fluid flow and geomechanical simulation to first calculate the three-dimensional stress evolution during a hypothetical CO_2 injection operation and then evaluate the probability of shear slip considering the statistical fracture distribution and a Coulomb failure analysis. We evaluate the probability of shear slip at different points within the injection zone and in the caprock just above the injection zone and relate this to the potential for opening of new flow paths through the caprock. Our analysis showed that a reverse faulting stress field would be most favorable for avoiding fracture shear reactivation, but site-specific analyses will be required because of strong dependency of the local stress field and fracture orientations.

1. Introduction

Sequestering carbon dioxide in deep geological formations, such as in depleted oil reservoirs or deep saline aquifers, is a promising option for reducing carbon dioxide emissions (IPCC 2005; Holloway 2007; Bickle 2009). Hydrocarbon reservoirs that have contained resources for millions of years as well as a number of ongoing demonstration projects indicate that CO_2 geosequestration is technically feasible (Michael et al. 2010). However, apart from the issue of public acceptance, a number of technical hurdles still need to be resolved before deploying the deep geologic storage of CO_2 at a scale that could make a significant contribution in reducing CO_2 emissions to the atmosphere. Technical challenges include the accurate estimation of storage capacity, characterization of storage sites, monitoring and confirmation of injected CO_2, and detection and prevention of CO_2 leakage to the biosphere. For example, microseismic events that may occur during CO_2 injection could affect the caprock integrity, and the effectiveness of the CO_2 geosequestration itself (Zoback and Gorelick 2012). Moreover, the potential for leakage may be impacted by injection-induced geomechanical changes, such as stress and deformations affecting fractures and permeability; thus, it is important to analyze such changes to ensure the security of industrial-scale CO_2 storage sites (Yamamoto and Takahashi 2004; Hawkes et al. 2005; Rutqvist 2012).

Four different trapping mechanisms can contribute to storing CO_2 in a deep reservoir: (1) structural and stratigraphic trapping, (2) residual CO_2 trapping, (3) solubility trapping, and (4) mineral trapping (IPCC 2005; Bachu 2008; Benson and Cole 2008; Zahid et al. 2010). The principal means for storing CO_2 is structural and stratigraphic trapping, in which low-permeability caprock prevents CO_2 from migrating to the surface. Structural traps are the result of crust movement whereas stratigraphic traps are the result of depositional or diagenetic processes. In residual trapping, CO_2 is immobile because of the interfacial tension between CO_2 and the formation water resulting from disconnected gas bubbles being left in the wake of a migrating stream of CO_2. Solubility and mineral trapping are collectively called chemical trapping, which occurs when CO_2 adsorbs onto organic materials contained on coals and shales or dissolves within subsurface fluid. CO_2 can then be involved in chemical reactions with the rock matrix, resulting in stable carbonate minerals, which are the most permanent form of geological storage (IPCC 2005; Bachu 2008). While structural and stratigraphical trapping and residual trapping are dominant in the early stages of CO_2 storage (on the order of hundreds to thousands of years), chemical trapping becomes more dominant at later stages. The reaction of dissolved CO_2 with minerals can be rapid (days) in the case of some carbonate minerals, but slow (hundreds to thousands of years) in the case of silicate minerals (IPCC 2005). It is important to note that the dissolution and precipitation of minerals can alter the frictional properties and permeability of fractures; therefore, the role of such chemical reactions in the mechanical and hydraulic behavior of fractures is important in evaluating the feasibility of CO_2 storage (Singuringdy and Berkowitz 2005; Yasuhara et al. 2006; Min et al. 2009, Rutqvist 2012). Numerical modeling has also been conducted to take into account the reactive solute transport in coupled fluid flow and geomechanical analysis (Taron et al. 2009; Kvamme and Liu 2009).

The geomechanical integrity of CO_2 reservoirs is important for the function of structural and stratigraphic trapping mechanisms. Injection-induced mechanical stress and deformation at depth can also result in ground heave, a phenomenon that might be detectable by geodetic monitoring. For example, at the In Salah CO_2 storage project in Algeria, the first few years of injection resulted in an observed ground heave of approximately 5 mm/year, affecting an area extending several kilometers from each injection well (Rutqvist et al. 2010). In addition, the increased reservoir pressure could potentially result in the reactivation of fractures that might exist within

and around the injection zone. The reactivation of existing fractures in a capping formation above the injection zone could result in dilatant fracture opening and enhanced permeability (Min et al. 2004), which could, in turn, lead to an enhanced upward CO_2-fluid migration. Shear reactivation along fractures or minor faults might also result in microseismic events or even events that might be felt by the local population (Zoback 2010; Rutqvist 2012). Events associated with CO_2 injection are analogous to those occurring during the stimulation of geothermal reservoirs, which are usually explained by the mechanisms of shear slip within small fractures (Moeck et al. 2009). It is difficult to predict how much permeability would change upon the reactivation of fractures and is at least equally difficult to quantify the CO_2 leakage resulting from such permeability changes. Therefore, the monitoring and analysis of both surface deformation and seismicity from the start of injection can be useful for constraining geomechanical models and predicting the potential for fracture reactivation in future injection scenarios (Rutqvist 2012). A conservative approach might be to design CO_2 injection in such a way that fracture reactivation could be avoided, thereby ensuring that the permeability of the caprock would remain essentially unchanged during the injection.

Characterizing and quantifying the potential for fracture reactivation in terms of shear slip have been the subject of a number of previous studies (Morris et al. 1996; Alaniz-Alvarez et al. 1993; Ito and Hayashi 2003). Morris et al. (1996) introduced the concept of slip tendency analysis, defining slip tendency (T_s) as the ratio of shear stress to normal stress on a plane. They defined T_{sMAX} as the maximum value of T_s at a given stress condition and analyzed slip tendency for all possible orientations of fractures in terms of the ratio T_s/T_{sMAX}. Morris et al. (1996) applied this concept to investigate the potential for reactivation of major faults at a depth of 5 km below Yucca Mountain in the United States. Ito and Hayashi (2003) used a similar analytical-solution approach to estimate possible fracture orientations that could result in shear slip, thereby impacting the performance of hot dry rock (HDR) geothermal reservoirs. They calculated shear slip and sheared-fracture surface rupture area by approximating the Coulomb failure line using a series of circles of different radii. Alaniz-Alvarez et al. (1998) developed and applied a so-called slip-rupture graph technique, in which the Coulomb failure criterion was used to determine the possibility of both slip along existing fractures and failure of the intact rock. If the principal stress difference (i.e., the difference between maximum and minimum compressive principal stress) required for fracture shear slip along existing fractures is larger than the stress difference necessary to make a new fracture, then a new fracture plane will be created. This could happen if the pre-existing plane was not optimally oriented for shear slip failure while the shear strength of the intact rock is exceeded. Finally, Rutqvist et al. (2008) proposed the concept of pressure margin in analyzing the potential for both tensile and shear failures in a CO_2 sequestration reservoir. They defined pressure margin as the fluid pressure minus the critical fluid pressure for failure, thereby indicating a safety margin for the maximum injection pressure. However, although the aforementioned studies were used to investigate the potential for fracture reactivation, they did not consider the fracture statistical distribution and, therefore, did not provide a quantitative analysis for fracture shear-slip probability under specific stress conditions.

The main focus of this paper is to develop and demonstrate an approach for probabilistic fracture-reactivation analysis associated with underground CO_2 injection and storage. We demonstrate this approach for a generic caprock-reservoir system based on the geometry and properties from Rutqvist and Tsang (2002) and, in one case, using fracture statistical data from a CO_2 storage site. Our approach involves coupled multiphase fluid flow and geomechanical simulations, first to calculate the stress evolution during a hypothetical CO_2 injection operation, and then to evaluate the probability of shear slip considering the statistical fracture distribution and a Coulomb failure analysis. These simulations are conducted using the TOUGH-FLAC simulator (Rutqvist et al. 2002; Rutqvist 2011) for three different stress regimes (normal, reverse, and strike-slip faulting)

as well as with fracture orientations generated using the Latin Hypercube Sampling (LHS) method. We evaluate the probability of shear slip at different points within the injection zone and in the caprock just above the injection zone, from which we draw conclusions related to the potential for the opening of new flow paths through the caprock. Consequently, the main contribution of this research is a quantitative analysis of fracture reactivation during CO_2 injection using a statistical distribution of fracture orientation.

2. Methodology

For this study, we first conducted a coupled multiphase fluid flow and geomechanical analysis to identify hydromechanical changes and calculate the stress evolution induced by CO_2 injection; we then investigated the probability of reactivating fractures. Fractures were virtually generated, and the probability of fracture shear slip was calculated based on the effective stress from the numerical analysis and generated fracture orientation.

2.1 Numerical code

TOUGH-FLAC is a numerical simulator based on linking the two computer codes TOUGH2 (Pruess et al. 1999) and FLAC3D (Itasca 2009). TOUGH2, developed at the Lawrence Berkeley National Laboratory (LBNL), is widely used for modeling heat transfer and multiphase, multicomponent fluid flow in applications such as geologic CO_2 storage. FLAC3D, developed by ITASCA^{TM}, is a well-known finite difference program for soil and rock mechanics—a powerful tool for describing the mechanical behavior of soil and rocks. The two codes are sequentially coupled, and the TOUGH-FLAC simulation runs seamlessly for coupled analysis (Rutqvist, 2011).

Fig. 1 shows the principal couplings between TOUGH2 and FLAC3D (Rutqvist 2011). For a specific problem, the two codes are linked through a central THM model for passing parameters between the two codes. The simulation progresses in time along with the multiphase fluid flow simulation in TOUGH2, with FLAC3D invoked intermittently, when desired, for a quasi-static mechanical calculation. For example, in the standard version, FLAC3D is called once each TOUGH2 time step. After a TOUGH2 time step, temperature (T), fluid pressure (P_l), gas pressure (P_g), and fluid saturation (S_l) are passed from TOUGH2 to FLAC3D elements. These parameters are passed directly to the FLAC3D elements via FLAC3D FISH—a programming capability in FLAC3D that facilitates linking the two codes (Itasca 2009). When updating these parameters in FLAC3D, the mechanical state is set in disequilibrium due to the internal changes induced (for example) by thermal strain and effective stress changes. A quasistatic mechanical simulation step in FLAC3D then takes it to a new mechanical equilibrium with an updated stress state. The new stresses and/or accumulated strain changes are then used to update the porosity and permeability within the TOUGH2 multiphase flow simulation. A detailed description of the simulator and its recent applications can be found in Rutqvist (2011).

2.2 Verification

To verify and gain confidence in the numerical approach and analysis of this particular case, we conducted two independent code verifications relevant to fluid injection and coupled hydromechanical responses in reservoirs. In order to verify the TOUGH2 code for modeling fluid injection, we conducted a two-dimensional well-pumping test simulation and compared the

numerical results with the Theis solution (Theis 1935). Eq. 1 is the drawdown at the point where the distance from the well is r.

$$h_0 - h = s = \frac{Q}{4\pi t} \int_{r^2 S/4Tt}^{\infty} \frac{e^{-z}}{z} dz \tag{1}$$

where h_0 is the initial head, h is the head at time t, s is the drawdown, Q is the constant pumping rate, T is transmissivity, and S is storativity. A semi-infinite one-dimensional model was used to conduct the numerical analysis; Table 1 shows the properties and initial conditions used for the verification. Fig. 2 shows the drawdown versus distance from the pumping well at a specific time. The numerical results match the analytical solution nearly perfectly.

To verify TOUGH-FLAC for coupled hydromechanical (poro-elastic) reservoir responses, we conducted a uniaxial consolidation analysis and compared the numerical results with Terzaghi's solution (Terzaghi 1923). If mechanical loading (P) is applied suddenly at the upper boundary of the one-dimensional saturated poroelastic media, the height of which is h, the pore pressure (P_p) at height z and time t is given as follows (Jaeger et al. 2007):

$$P_p(z,t) = \frac{\alpha MP}{(\lambda + 2G + \alpha^2 M)} \sum_{n=1,3,\ldots}^{\infty} \frac{4}{n\pi} \sin(\frac{n\pi z}{2h}) \exp(\frac{-n^2\pi^2 kt)}{4\mu Sh^2}) \tag{2}$$

where α is the Biot constant (Biot 1941), M is the Biot modulus, λ is the Lame constant, G is the shear modulus, k is permeability, μ is fluid viscosity, and S is the storage coefficient. Eq. 3 is the vertical displacement (w) at the upper boundary versus time:

$$w(0,t) = \frac{-Ph}{(\lambda + 2G)} [1 - \frac{\alpha^2 M}{(\lambda + 2G + \alpha^2 M)} \sum_{n=1,3,\ldots}^{\infty} \frac{8}{n^2\pi^2} \exp(\frac{-n^2\pi^2 kt}{4\mu Sh^2})] \tag{3}$$

Fig. 3 shows a schematic view and the boundary conditions of the numerical model; Table 2 shows the properties used for the verification of the consolidation analysis.

After mechanical loading, we applied undrained pore pressure as an initial condition. Fig. 4(a) shows the evolution of pressure at the lower boundary whereas Fig. 4(b) shows the evolution of displacement at the upper boundary. The numerical results are in close agreement with the analytical solution.

2.3 Numerical model of geological CO_2 storage system

Fig. 5 shows a schematic view of our model. We simulated the injection of CO_2 into a 300 m thick injection zone (storage reservoir) located between 1200 and 1500 m depth. The overburden consists of a 1000 m thick upper layer and a 200 m thick caprock located just above the injection zone. The exact location of the CO_2 injection point is 1460 m in depth. Although the model was set up in three dimensions, the analysis was conducted effectively in two dimensions, with no-flow and no-displacement boundary conditions imposed in the direction normal to the model.

Over a ten-year period, CO_2 was injected at a constant flow rate of 0.05 kg/s per meter normal to the model plane (Rutqvist and Tsang 2002). This flow rate is equivalent to 1.6 Mt/year if the injection were conducted along a 1000 m thick section of the reservoir normal to the model plane, which would, for example, represent the injection rate for a 1 km long horizontal well. We can also relate this to real injection rates at the In Salah CO_2 storage project, where injection rates have been 0.5 to 1.0 million tons per year distributed over 3 horizontal injection wells, each of which is 1 to 1.5 km long (Rutqvist et al. 2010). To minimize boundary effects, we locate the lateral boundaries sufficiently far from the CO_2 injection point.

Material properties and boundary conditions are presented in Table 3 and Fig. 6, respectively. The reservoir is assumed to behave elastically, and horizontal displacement is fixed only on the lateral boundaries, whereas vertical displacement is fixed at the bottom. For the hydraulic and thermal boundary conditions, the ground-surface temperature and pressure are set to 10°C and 0 Pa, respectively. A thermal gradient of 25°C/km and hydrostatic pressure are assumed leading to a temperature and pressure at the lower boundary of 60°C and 19.62 MPa, respectively.

2.4 Probabilistic fracture reactivation analysis

For the fracture reactivation analysis, we generated two types of fracture-orientation data sets: one for random fracture orientation and another for actual fracture orientation based on field data. The Latin Hypercube Sampling (LHS) method, developed by McKay, Conover, and Beckman (McKay et al. 1979), was used to generate fractures. This method is similar to the Monte Carlo method, in that it is used to select n different values from each of k variables. However, the Monte Carlo method randomly selects n different values based on the probability of a cumulative distribution function (CDF); as such, it yields reasonable values only if the value of n is quite large. Thus, to increase the efficiency of the sampling method, the LHS method makes selections in each of the nonoverlapping intervals based on the equal probability of CDF, providing reasonable values even when the value of n is relatively small. In addition, the values of n associated with certain variables were paired with the values of n associated with other variables in a random manner, until an $n \times k$ matrix was formed.

As a first type of data set, random orientations were generated based on a probability distribution function (PDF) with a uniform distribution of orientation. A second type of data set was chosen using published actual fracture statistics related to the In Salah project (Iding and Ringrose 2010; Smith et al. 2011). The PDF of the actual fracture data from In Salah has a Fisher distribution function that has orientations distributed around a mean orientation. Ten thousand fractures were generated for both the cases of random fracture orientations and the actual fracture orientations. Fig. 7 shows the distribution of the generated orientations in an equal area net.

The data from the In Salah site are listed in Table 4. At In Salah, the dominant fracture orientation is a NW-SE strike with a variation of about 15°, with an almost vertical dip angle. In our analysis, we assumed a constant Fisher distribution (κ) of 150, which means that the deviation angles of approximately 99% of the fractures are less than 15°.

Fig. 8 shows a flow chart for calculating the probability of shear slip. We developed a program to generate fracture orientations and calculate the probability of shear slip, with the code divided into two parts: a part that generates the fracture orientation using the LHS method and a part that conducts a probabilistic analysis of shear slip. In the sampling part, we generated virtual fractures using two kinds of fracture distribution—namely, Fisher and uniform distributions. The information on the number of fractures, Fisher constant, and mean dip/dip direction were needed

for the Fisher distribution whereas only the number of fractures was required for uniform distribution. In the analysis part, normal and shear stresses for each fracture orientation were calculated using fracture orientations and stresses based on the numerical analysis. More detailed information on discrete fracture networks was not incorporated in the current analysis, such as the spatial distribution, size, shape, and connectivity of fractures. In this sense, the current study is a conservative one, given the consequences of leakage and the uncertainty associated with obtaining detailed fracture information at a given CO_2 reservoir likely to be located at a depth of 1 to 2 km.

To evaluate the probability of shear slip of generated fractures, we adopted a Coulomb failure criterion (assuming zero cohesion), as follows:

$$\tau = \mu \cdot \sigma \tag{4}$$

where τ is shear stress, σ is the stress normal to the fracture, and μ is the coefficient of friction. According to this failure criterion, shear slip occurs if shear stress is greater than the normal stress multiplied by the coefficient of friction.

Fig. 9 shows that the normal stress and the shear stress that act on a given plane depend on the orientation of the plane. When a stress field is defined by a stress tensor, the stress vector acting on a plane with normal vector $\boldsymbol{n}$ can be calculated using Cauchy's formula (Jaeger et al. 2007).

$$\boldsymbol{T}_j = \sigma_{ij}\boldsymbol{n}_i \tag{5}$$

where $\boldsymbol{T}_j$ is the traction vector, σ_{ij} is the stress tensor, and $\boldsymbol{n}_i$ is the normal vector of the fracture plane. The magnitude of the normal stress σ and shear stress τ of any stress vector $\boldsymbol{T}$ acting on an arbitrary plane with normal vector $\boldsymbol{n}$ at a given point is expressed as follows:

$$\sigma = \boldsymbol{T} \cdot \boldsymbol{n} \tag{6}$$

$$\tau = \sqrt{(\boldsymbol{T}^2 - \sigma^2)} \tag{7}$$

Thus, when the orientation of a fracture and the stress field is given, normal and shear stress acting on the fracture plane can be determined. Using these normal and shear stress values, we can determine whether shear failure occurred at a specific orientation. The probability of fracture shear slip was calculated as the number of fractures failed in shear, divided by the total number of generated fractures.

To investigate the shear slip potential at a specific point, we selected four points within the reservoir and the caprock, as shown in Fig. 10. Point A is the CO_2 injection point, Point B is located horizontally 1000 m away from the CO_2 injection point, Point C is located 50 m above the lower boundary of the caprock, and Point D is located 50 m below the upper boundary of the caprock. Three kinds of stress regimes were considered: (1) normal faulting, (2) reverse faulting, and (3) strike-slip faulting (Fig. 11). At depths below 1000 m, the ratio of horizontal stress to vertical stress (k) has been observed to range between 0.5 and 2.0 (Brown and Hoek 1978). In this

study, vertical stress was fixed as gravitational stress, and horizontal stresses were chosen to be 0.5, 0.75, 1.5, or 2.0 times the vertical stress, depending on the stress regimes. Thus, vertical stress is the maximum, minimum, and intermediate principal stress in normal faulting, reverse faulting, and strike slip faulting regimes, respectively. The friction coefficient used for this study was 0.6, which is the lower bound of typical values (Byerlee 1978).

3. Results

3.1 Ground heaving induced by CO_2 injection

We simulated the injection of CO_2 at a constant flow rate of 0.05 kg/s per meter (per meter normal to model; Rutqvist and Tsang 2002) over a 10-year period. This flow rate is equivalent to 1.6 Mt/year, if the injection were conducted along a 1000 m thick section of the reservoir normal to the model. Fig. 12 shows the evolution of pressure near the injection point. The maximum pore pressure near the injection point is about 26 MPa after 10 years of injecting CO_2. Because the permeability of the caprock and the basement is four orders of magnitude lower than that of the aquifer, the injected CO_2 spreads primarily in a horizontal direction.

Fig. 13 shows the vertical displacement profile after 30 days, one year, three years, six years, and 10 years. The changes in effective stress induced by the increase in pore pressure result in the poroelastic expansion of the reservoir and the uplifting of the ground surface (Rutqvist and Tsang 2002). The maximum vertical displacement after 10 years is approximately 0.88 m—in other words, 88 mm/year; this large value results from the reservoir thickness of 300 m and a relatively low elastic modulus of 5 MPa. In comparison, only about 5 mm/year of uplift has been observed at the In Salah CO_2 storage project, which has a reservoir formation of only 20 m in thickness (Iding and Ringrose 2010). The investigation of uplift is a good measure of reservoir performance, in that it can both (1) be an effective monitoring activity and (2) potentially have an impact on surface structures. Moreover, in a field situation, the observed ground-surface heave can be used to constrain the value of the elastic modulus of the reservoir.

The maximum vertical displacement can be roughly calculated using a simplified uniaxial vertical displacement model. If the lateral extent of the reservoir is much larger than its thickness, the reservoir responds as if it were laterally confined, and the vertical displacement can be calculated as follows (Fjaer et al. 2008):

$$\frac{\Delta h}{h} = \frac{1}{E}\frac{(1+\nu)(1-2\nu)}{1-\nu}\alpha\Delta P \tag{8}$$

where E is the elastic modulus, ν is poisson's ratio, α is the Biot coefficient, ΔP is the increment of pore pressure, Δh is the vertical displacement, and h is the thickness of the aquifer.

Eq. 8 can be used to estimate vertical displacement with the change in reservoir pore pressure. For example, when the maximum pore pressure from the numerical result was used, the calculated vertical displacement using Eq. 8 was about 1.07 m after 10 years, which is about 20%

higher than the numerically calculated value. Similarly, in the case of In Salah, the measured and numerically calculated vertical displacement was about 2.5 cm, while vertical displacement using the uniaxial strain model was about 3 cm (Rutqvist 2012). The uniaxial model overestimates the vertical displacement compared to the real case or numerical results as the pore pressure is not distributed uniformly in the reservoir, unlike the assumption in Eq. 8. Another factor is that the overburden stiffness, which tends to restrict vertical deformation in a real three-dimensional situation, is not considered in the uniaxial strain model of Eq. 8.

Fig. 14 shows the calculated vertical displacement for both the uniaxial strain model and numerical modeling. The thickness of the aquifer in this example was set at 100 m, with other properties kept the same, as shown in Table 3. In this figure, uniaxial displacement is calculated using the maximum reservoir pressure from the numerical modeling. Vertical displacement of the uniaxial strain model and vertical displacement at the top of the aquifer were rather similar (within 5%), whereas greater differences were observed when comparing vertical displacement at the surface. As the thickness of the overburden increases, the vertical displacement at the surface decreases. Therefore, the discrepancies between the numerical model and uniaxial strain model can be explained mainly by the stiffness of the overburden and, to a lesser degree, by the non-uniform pore pressure. Finally, differences in the boundary conditions for the uniaxial strain model and our numerical model can also have an impact. Because the lateral boundary condition was not a precisely fixed displacement condition, the generated lateral stress was less than the theoretical one, which resulted in slightly smaller vertical displacement.

3.2 Evolution of effective stress

Fig. 15 shows the evolution of the increments of total stress and pore pressure at points A, B, C, and D. Total stress increases in the horizontal direction occur proportional to the pore pressure increase, while a much smaller increase in total stress occurs in the vertical direction because of the free vertical displacement condition at the ground surface. The increase in lateral stress is caused by poroelastic stress, which has been observed in oil fields and also in coupled geomechanical modeling (Hillis 2003; Rutqvist 2012). In this study, the magnitude of the increased total stress in the horizontal direction is approximately half the increased pore pressure. Pore pressure increases at Point C and Point D, located in the caprock, amount to 8 MPa and 3 MPa, respectively, although the permeability of the caprock is lower than that of the reservoir by four orders of magnitude.

Using the Mohr circle for stress representation, we investigated the effective stress change at Points A through D (Figs. 16 to 19). At the initial state of normal and strike-slip stress regimes, there were fractures with the potential for shear slip in the current stress field, meaning that these fractures were critically stressed for shear slip (Zoback et al. 2002). After 10 years of CO_2 injection, the Mohr circle moved to the left regardless of the stress regime, and there was an increase in the area that reached failure. The size and location of the Mohr circle and the size of the failed area are different depending on the stress regime because the magnitude of effective stress changes is different for horizontal and vertical directions. The size of the Mohr circle decreases in the case of a normal faulting stress regime, increases in the case of a reverse faulting stress regime, and both decreases and increases in the case of a strike-slip faulting regime. The amount of decreased effective stress is highest for the vertical direction, which has a significant impact on the shear-slip potential.

3.3 Probability of fracture reactivation

To quantitatively investigate the probability of fracture reactivation, we calculated the probability using virtually generated fracture orientations and the effective stress evolution. Fig. 20 shows the evolution of fracture shear slip probability for the three different stress regimes at Point A and Point B during CO_2 injection. In all cases, the probability increases with the injection of CO_2. When the fractures are distributed randomly, the maximum probability of fracture shear slip after 10 years of CO_2 injection at Point A is about 40% for a normal faulting stress regime, 40% for a reverse faulting stress regime, and 70% for a strike-slip stress regime. In the case of fracture statistics derived from In Salah, the probability of the fracture shear slip is almost 100% for the normal faulting stress regime, while fracture shear slip did not occur in the reverse faulting stress regime case. Moreover, under the assumed stress magnitudes, all fractures were calculated to slip for the strike-slip faulting stress regime both before and after the injection of CO_2.

Fig. 21 shows the evolution of the fracture shear slip probability at Point C and Point D, located in the caprock. In all cases, the probabilities of fracture shear slip at Points C and D in the caprock are lower than at Points A and B in the reservoir. Fracture shear slip at Points C and D did not occur for the normal faulting stress regime, even when the fracture–shear–slip probability at Point A is almost 100% in the fracture statistics derived from In Salah. Because Point D is located in the upper part of the caprock, the pressure increase is less than 3 MPa (Fig. 15), which is insufficient to induce any substantial increase in the probability of fracture shear slip. Although the pressure increase at Point C is somewhat larger, it was not sufficient to induce fracture shear slip. To explain the shear slip mechanism more effectively, we used a stereonet to plot the actual orientation data, together with the possible range of orientations that can be allowed for shear slip at Points A through D (Figs. 22 to 25). The red area is the distribution of fractures over which shear slip can occur; the black points are the actual orientation data from the In Salah fracture data set. Our analysis of the stereonet shown in Figs. 22 to 25 indicates why such large differences in shear-slip potential occur depending on the stress regime, especially with the actual orientations in the In Salah fracture data set. As shown in Figs. 22 to 25, no overlapping area occurs between the shear-slip area and actual fracture orientation for the reverse faulting stress regime. In the case of the In Salah fracture data set, the majority of the fractures were not vulnerable to shear slip even under more substantial pore pressure, because of the presence of near-vertical fractures. However, most fractures were located in the shear slip area for the strike-slip faulting stress regime, resulting in a high probability of fracture shear slip. The reverse faulting stress regime had the least probability of a fracture shear slip, mainly due to the highest minimum principal stress being vertical. As already shown in Fig. 16, the minimum principal stress of the reverse faulting stress regime is greater than that of other stress regimes; consequently, the Mohr circle does not meet the failure criterion.

Based on this observation, the reverse faulting stress regime seems to provide the most suitable conditions for CO_2 geosequestration among the three kinds of stress regimes considered in this study. However, this result must be interpreted with caution. If a site has fracture sets that are vulnerable to shear slip for the reverse faulting stress regime, the probability of shear slip may become the greatest for a reserve faulting stress regime. In other words, the probability of fracture shear slip is site specific, and it is a function of both the local stress field and orientations of the fractures. In addition, the magnitudes of shear stress, as dictated by the stress ratio in each stress regime in this study, were upper-bound values; it is a conservative choice with respect to the potential for fracture shear slip. If the ratio of stress, i.e., the ratio of vertical to horizontal stress or ratio of the minimum to maximum horizontal stresses, approaches unity, the probability of shear slip dramatically decreases regardless of the stress regime, and the distinction of different

stress regimes may not be meaningful. Therefore, a site-specific study must be conducted to investigate the actual probability of shear slip induced by CO_2 injection.

3.4 Effect of caprock permeability

In our numerical model, the permeability of the caprock is lower than that of the aquifer by four orders of magnitude. This value of caprock permeability (1×10^{-17} m^2) probably belongs to the higher end of the typical range; therefore, the results presented in this study can be considered to be conservative. In order to investigate the effect of caprock permeability, additional analyses were conducted by varying the caprock permeability from 1×10^{-17} m^2 to 1×10^{-20} m^2. Fig. 26 shows the evolution of pore pressure at Point C with different caprock permeability. If the caprock permeability is lower than 1×10^{-19}, the pore pressure at Point C increases less than 1 MPa after 10 years of CO_2 injection, which means that the caprock effectively prevents the upward migration of injected CO_2.

Fig. 27 shows the probability of fracture shear slip at Point C, with random fracture orientations for different caprock permeability. In all cases, the probability of fracture shear slip decreases with the decrease in caprock permeability, which consequently means that the potential for CO_2 leakage decreases. As expected, the permeability of caprock plays a significant role in controlling the shear slip in the caprock.

It is worth noting that the reactivation of fractures in the reservoir and caprock does not necessarily result in the leakage of CO_2 due to the requirement that fractures must have a high degree of connectivity through the lower and upper parts of the caprock. In addition, the actual magnitude of permeability increases in the reactivated fractures was not quantified in the current approach. Further work is therefore suggested to incorporate the connectivity of fractures into the fracture reactivation analysis as well as quantify fracture permeability after shear slip in both the caprock and reservoir.

4. Conclusions

We have developed and demonstrated an approach for probabilistic fracture-reactivation analysis associated with underground CO_2 injection and storage. We demonstrated the approach for a generic caprock-reservoir system in one case using published fracture statistics from the In Salah CO_2 storage project in Algeria. This analysis involved multiphase fluid flow and geomechanical simulations, first calculating the stress evolution during a hypothetical CO_2 injection operation and then evaluating the probability of shear slip considering the statistical fracture distribution and a Coulomb failure analysis. In addition to the fault slip analysis, we studied injection-induced ground-surface deformations and found that quite a substantial ground-surface uplift could result from the assumed elastic properties and the relatively thick injection zone. Monitoring and modeling of such uplift could be used to estimate the underground reservoir pressure evolution and constrain *in situ* elastic properties for the geomechanical model.

The conclusions of this study are summarized as follows:

- After 10 years of injection, the reservoir pore pressure increased by about 12 MPa near the injection point, which (according to the coupled numerical simulation) induced vertical ground-surface displacement of around 0.87 m. We also found that a simplified analytical uniaxial strain model could provide an approximate estimation of the surface

uplift, with some discrepancies related to non-uniform pressure distribution and the effects of overburden stiffness.

- Injection-induced changes in effective stress differ in vertical and horizontal directions because geometrical effects (e.g., laterally extensive reservoir and relative proximity to a free-moving ground surface) result in different total stress changes in vertical and horizontal directions. The decrease in effective stress is highest for the vertical direction—a finding that could be critical in evaluating the shear slip potential.
- Because the reverse faulting stress regime had a greater minimum principal stress than other stress regimes, there was less chance for shear failure in this stress regime. In fact, among the three types of stress regimes considered in this study, the reverse faulting stress regime was generally the most suitable for CO_2 geosequestration, leading to the least probability of fracture reactivation.
- When caprock permeability is lower than 1×10^{-19}, pore pressure in the caprock increases by less than 1 MPa after 10 years of CO_2 injection, and fracture reactivation in the caprock is not likely to occur.

Finally, we conclude that the probability of fracture shear slip is a function of the stress field, injection pressure, and fracture geometry; thus, future site-specific studies should be conducted to investigate the probability of shear slip induced by CO_2 injection. The orientation of fractures was used as a key geometrical parameter in the current study; however, the mechanism of a fracture shear slip is not straightforward in the field as fracture shear slip is also affected by other factors, such as fracture size, roughness, fillings in the fractures, and connectivity of fractures. Fracture size within the reservoir and caprock will greatly affect the magnitude of fracture dilation. Connectivity will also play an important role in any shear slip, resulting in an actual increase in permeability and leakage. The current study is a conservative one, given the consequences of the leakage and the uncertainty associated with information regarding the discrete fracture network at a given CO_2 reservoir, which will likely be located at a depth of 1 to 2 km. Although characterization fractures at such a depth will be challenging, more elaborate analysis considering such factors will help in evaluating the feasibility of CO_2 storage in geological media. Moreover, an initially tight, low-permeability caprock could effectively delay pressure diffusion into the caprock, thereby preventing the reactivation of fractures across the caprock. Thus, if fractures are sealed with minerals, the likelihood of fracture reactivation could be much less. On the other hand, a few slightly permeable fractures might be susceptible to being breached, leading to an enhanced upward migration of CO_2. The difficulty lies in being able to quantify such an enhancement—which is also a subject for future research.

Acknowledgement

This research was supported by Basic Science Research Program through the National Research Foundation of Korea (NRF) funded by the Ministry of Education, Science and Technology (2010-0025206) and was conducted on behalf of the Ministry of Land, Transport and Maritime Affairs (MLTM) of Korean government under their “Development of Technology for CO_2 Marine Geological Storage” program. Additional support was provided by the U.S. Dept. of Energy under Contract No. DE-AC02-05CH11231. Editorial review by Dan Hawkes at Berkeley Lab is greatly appreciated.

References

Alaniz-Alvarez SA, Nieto-Samaniego AF, Tolson G (1998) A graphical technique to predict slip along a pre-existing plane of weakness. Engineering Geology 49: 53–60

Bachu S (2008) CO_2 storage in geological media: Role, means, status and barriers to deployment. Prog Energ Combust 34: 254–273

Benson SM, Cole DR (2008) CO_2 sequestration in deep sedimentary formations. Elements 4: 325–331

Bickle MJ (2009) Geological carbon storage. Nature Geosci 2: 815–818

Biot MA (1941) General theory of three-dimensional consolidation. J Appl Phys 12: 155–164

Brown ET, Hoek E (1978) Trends in relationship between measured in-situ stresses and depth. Int J Rock Mech Min Sci 15: 211–215

Byerlee J (1978) Friction of rocks. Pure Appl Geophys 116: 615–626

Fjaer E, Holt RM, Horsrud P, Raaen AM, Risnes R (2008) Petroleum related rock mechanics, 2nd edn. Elsevier Science

Hawkes CD, McLellan PJ, Bachu S (2005) Geomechanical factors affecting geological storage of CO2 in depleted oil and gas reservoirs. J Can Pet Technol 44:52–61Hillis RR (2003) Pore pressure/stress coupling and its implications for rock failure. Geological Society, London, Special Publications 216: 359–368

Holloway S (2007) Carbon dioxide capture and geological storage. Phil Trans Math Phys Eng Sci 365(1853): 1095–1107

Kvamme B, Liu S (2009) Reactive transport of CO_2 in saline aquifers with implicit geomechanical analysis. Energy Procedia 1:3267-3274

Iding M, Ringrose P (2010) Evaluating the impact of fractures on the performance of the In Salah CO2 storage site. Int J Greenhouse Gas Control 4: 242–248

IPCC (2005) Carbon dioxide capture and storage. Cambridge University Press, Cambridge

Itasca Consulting Group Inc. (2009) FLAC-3D Manual: Fast Lagrangian Analysis of Continua in 3 Dimensions version 4.0

Ito T, Hayashi K (2003) Role of stress-controlled flow pathways in HDR geothermal reservoirs. Pure Appl Geophys 160: 1103–1124

Jaeger JC, Cook NGW, Zimmerman RW (2007) Fundamentals of rock mechanics, 4th edn. Blackwell, London

McKay MD, Conover WJ, Beckman RJ (1979) A comparison of three methods for selecting values of input variables in the analysis of output from a computer code. Technomet 221: 239–245

Michael K, Golab A, Shulakova V, Ennis-King J, Allinson G, Sharma S, Aiken T (2010) Geological storage of CO2 in saline aquifers—A review of the experience from existing storage operations. Int J Greenhouse Gas Control 4: 659–667

Min KB, Rutqvist J, Elsworth D (2009) Chemically and mechanically ediated influences on the transport and mechanical characteristics of rock fractures. Int J Rock Mech Min Sci 46(1):80-89

Min KB, Rutqvist J, Tsang CF, Jing L (2004) Stress-dependent permeability of fractured rock masses: a numerical study. Int J Rock Mech Min Sci 41: 1191–1210
Moeck I, Kwiatek G, Zimmermann G (2009) Slip tendency analysis, fault reactivation potential and induced seismicity in a deep geothermal reservoir. J Struc Geol 31: 1174–1182
Morris A, Ferrill DA, Henderson DB (1996) Slip tendency analysis and fault reactivation. Geology 24: 275–278
Pruess K, Oldenburg C, Moridis G (1999) TOUGH2 User's Guide, Version 2.0. Lawrence Berkeley National Laboratory Report LBNL–43134
Rutqvist J, Tsang CF (2002) A study of caprock hydromechanical changes associated with CO2-injection into a brine formation. Environ Geol 42: 296–305
Rutqvist J, Wu YS, Tsang CF, Bodvarsson G (2002) A modeling approach for analysis of coupled multiphase fluid flow, heat transfer, and deformation in fractured porous rock. Int J Rock Mech Min Sci 39: 429–442
Rutqvist J, Birkholzer J, Cappa F, Tsang CF (2007) Estimating maximum sustainable injection pressure during geological sequestration of CO2 using coupled fluid flow and geomechanical fault-slip analysis. Energy Conv Manag 48: 1798–1807
Rutqvist J, Birkholzer JT, Tsang CF (2008) Coupled reservoir-geomechanical analysis of the potential for tensile and shear failure associated with CO2 injection in multi-layered reservoir-caprock systems. Int J Rock Mech Min Sci 45: 132–143
Rutqvist J, Vasco D, Myer L (2010) Coupled reservoir-geomechanical analysis of CO2 injection and ground deformations at In Salah, Algeria. Int J Greenhouse Gas Control 4:225–230
Rutqvist J (2011) Status of the TOUGH-FLAC simulator and recent applications related to coupled fluid flow and crustal deformations. Comput Geosci 37: 739–750
Rutqvist J (2012) The geomechanics of CO2 storage in deep sedimentary formations. Geotech Geol Eng 30(3):525-551
Singurindy O, Berkowitz B (2005) The role of fractures on coupled dissolution and precipitation patterns in carbonate rocks. Advances in Water Resources 28(5):507-521
Smith J, Durucan S, Korre A, Shi JQ, Sinayuc C (2011) Assessment of fracture connectivity and potential for CO2 migration through the reservoir and lower caprock at the In Salah storage site. Energy Procedia 4: 5299–5305
Taron J, Elsworth D, Min K-B (2009) Numerical simulation of thermal-hydrologic-mechanical-chemical processes in deformable fractured porous media. Int J Rock Mech Min Sci 46(5):842-854
Terzaghi K (1923) Die Berechnung der Durchlassigkeitsziffer des Tones aus dem Verlauf der hydrodynamischen Spannungserscheinungen. Sber Akad Wiss, Wien Math Naturwiss Kl Abt II A 132: 125–138
Theis CV (1935) The relation between the lowering of the piezometric surface and the rate and duration of discharge of a well using groundwater storage. Am Geophys Union Trans 16: 519–524

Yamamoto K, Takahashi K (2004) Importance of the geomechanics for the safety of CO2 geologic sequestration. Proceedings of 3rd Asian Rock mechanics symposium, Nov 30–Dec 2, 2004, Kyoto, Japan, 467-472

Yasuhara H, Polak A, Mitani Y, Grader AS, Halleck PM, Elsworth D (2006) Evolution of permeability through fluid-rock reaction under hydrothermal conditions. Earth Planet Sci Lett 244(1-2):186-200

Zahid U, Lim Y, Jung J, Han C (2010) CO_2 geological storage: A review on present and future prospects. Korean J Chem Eng 28: 674–685

Zoback MD, Townend J, Grollimund B (2002) Steady-state failure equilibrium and deformation of intraplate lithosphere. Int Geol Rev 44: 383–401

Zoback MD (2010) The potential for triggered seismicity associated with geologic sequestration of CO2 in saline aquifers. American Geophysical Union (AGU), EOS Trans AGU, 91(52), Fall Meeting, Suppl, Abstract NH11C-01

Zoback MD, Gorelick SM (2012) Earthquake triggering and large-scale geologic storage of carbon dioxide. Proc. National Academy of Sciences, doi:10.1073/pnas.1202473109

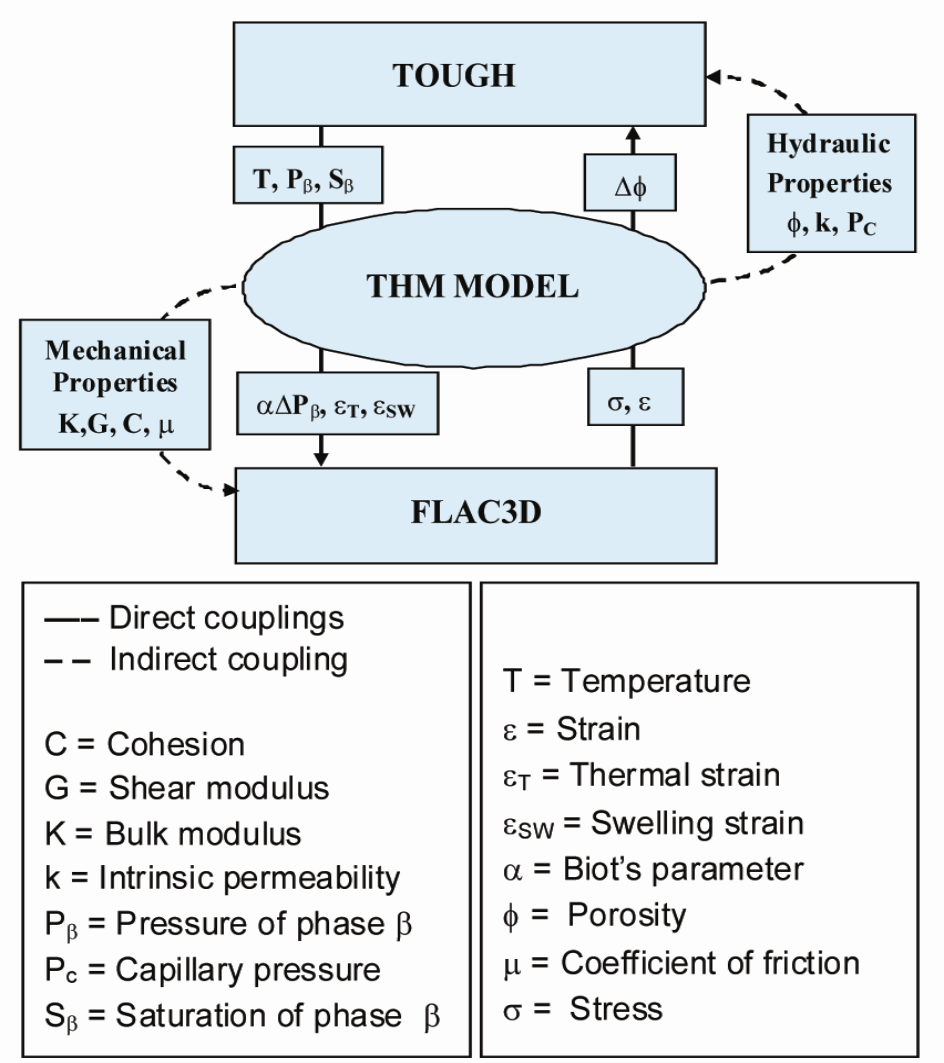

Fig. 1. Schematic of TOUGH2 and FLAC3D interactions for coupled multiphase and geomechanical simulations (Rutqvist 2011)

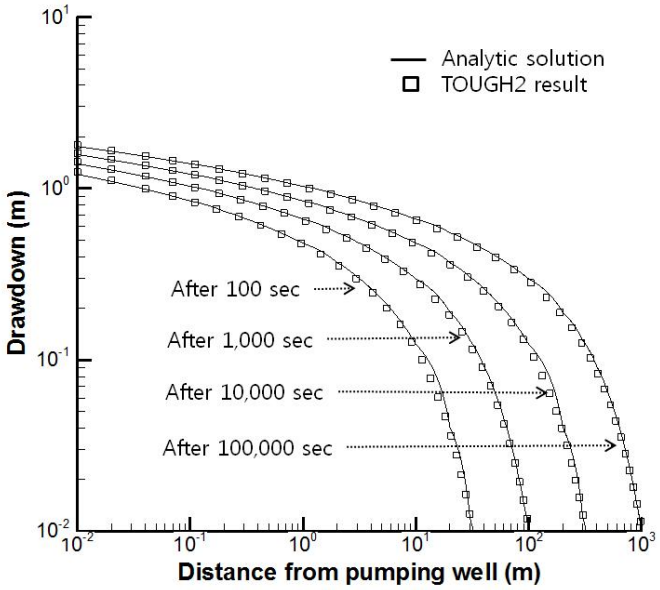

Fig. 2. Drawdown versus distance from the pumping well at a specific time

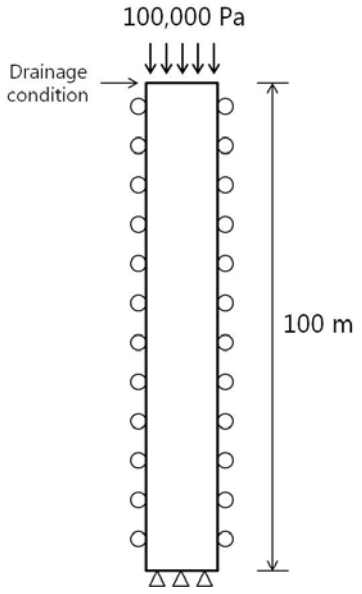

Fig. 3. Schematic view of the uniaxial consolidation model

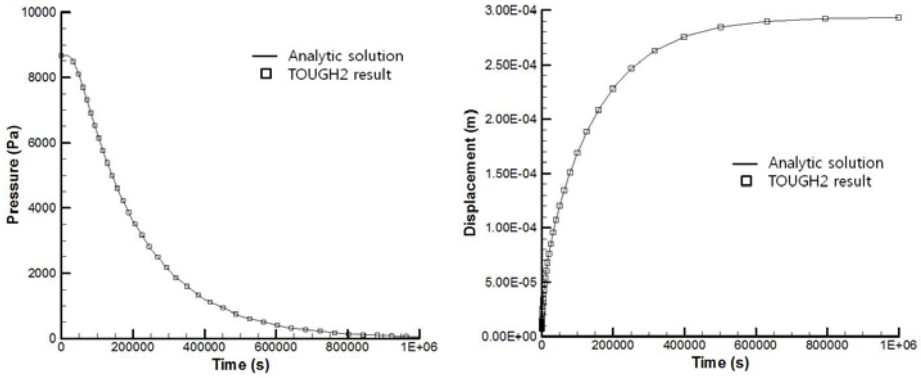

(a) (b)

Fig. 4. Results of the uniaxial consolidation analysis: (a) evolution of pressure at the lower boundary, (b) evolution of displacement at the upper boundary

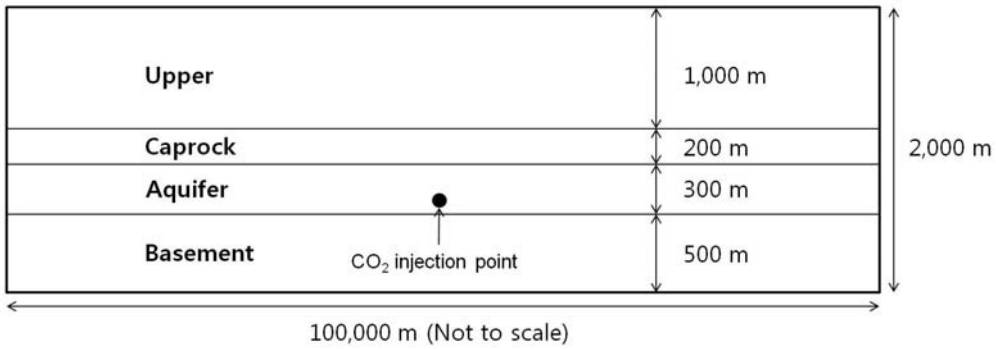

Fig. 5. Schematic view of the analysis model

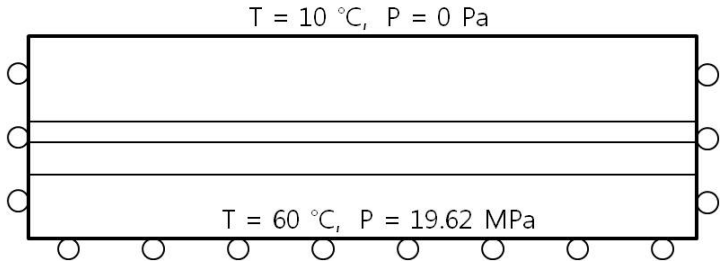

Fig. 6. Boundary conditions

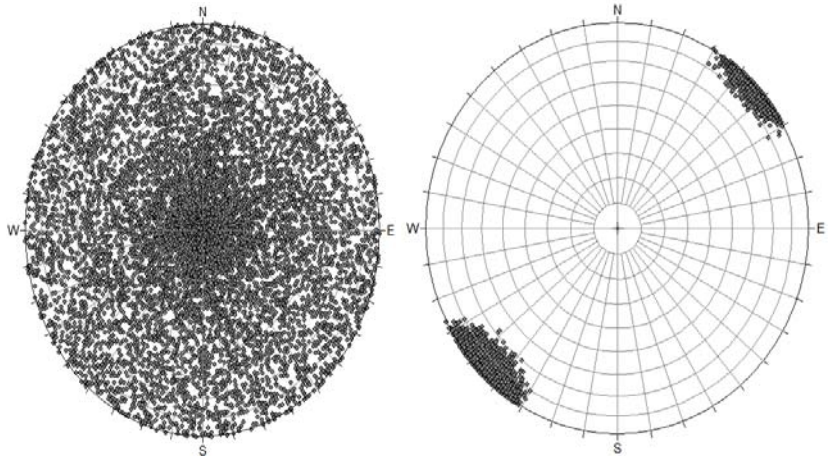

(a) (b)

Fig. 7. Distribution of 10,000 generated orientations in an equal area net: (a) random distribution of general data, (b) data from In Salah

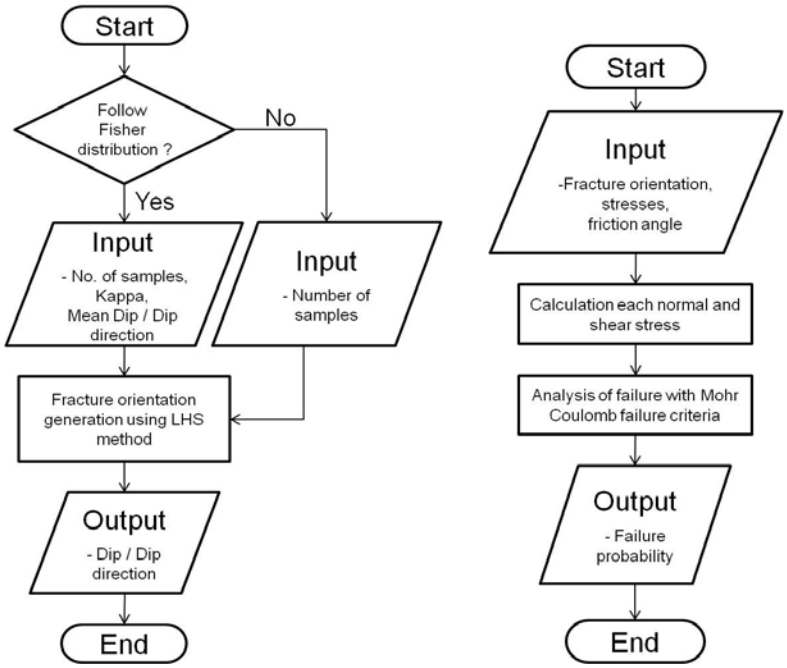

(a) (b)

Fig. 8. Flow chart for calculating the probability of shear slip: (a) sampling part, (b) analysis part

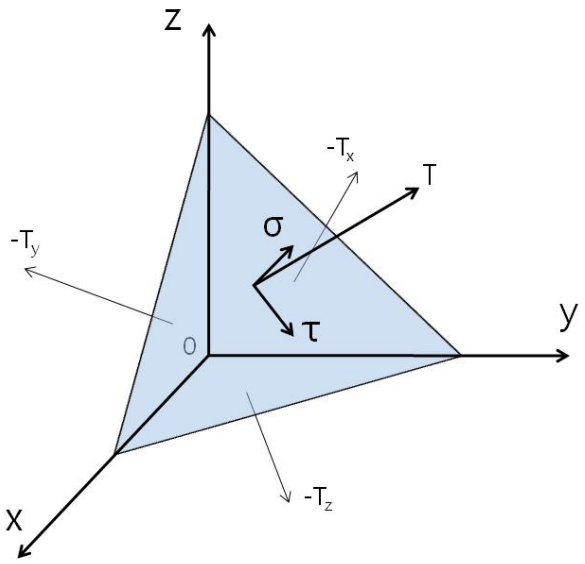

Fig. 9. Normal stress σ and shear stress τ acting on a given plane

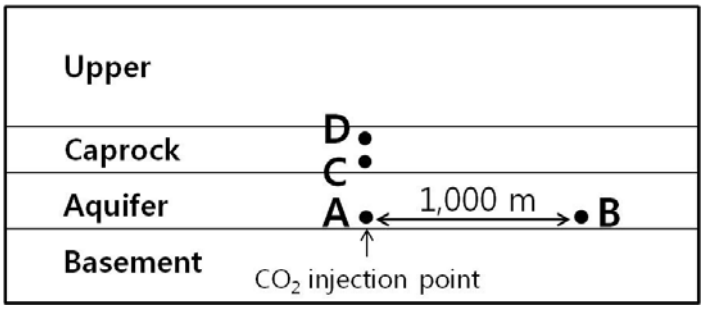

Fig. 10. Points selected for measurement

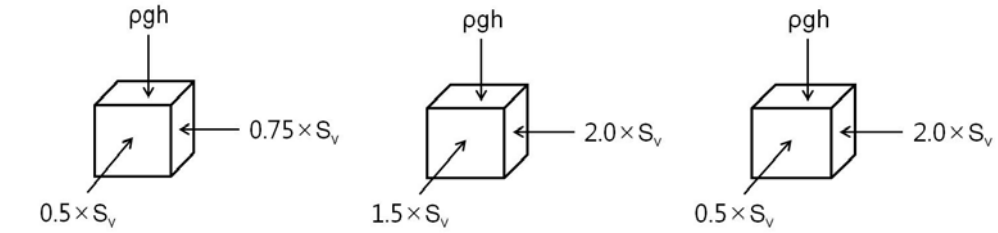

(a) (b) (c)

Fig. 11. *In situ* stress regime: (a) normal faulting stress regime, (b) reverse faulting stress regime, (c) strike slip faulting stress regime

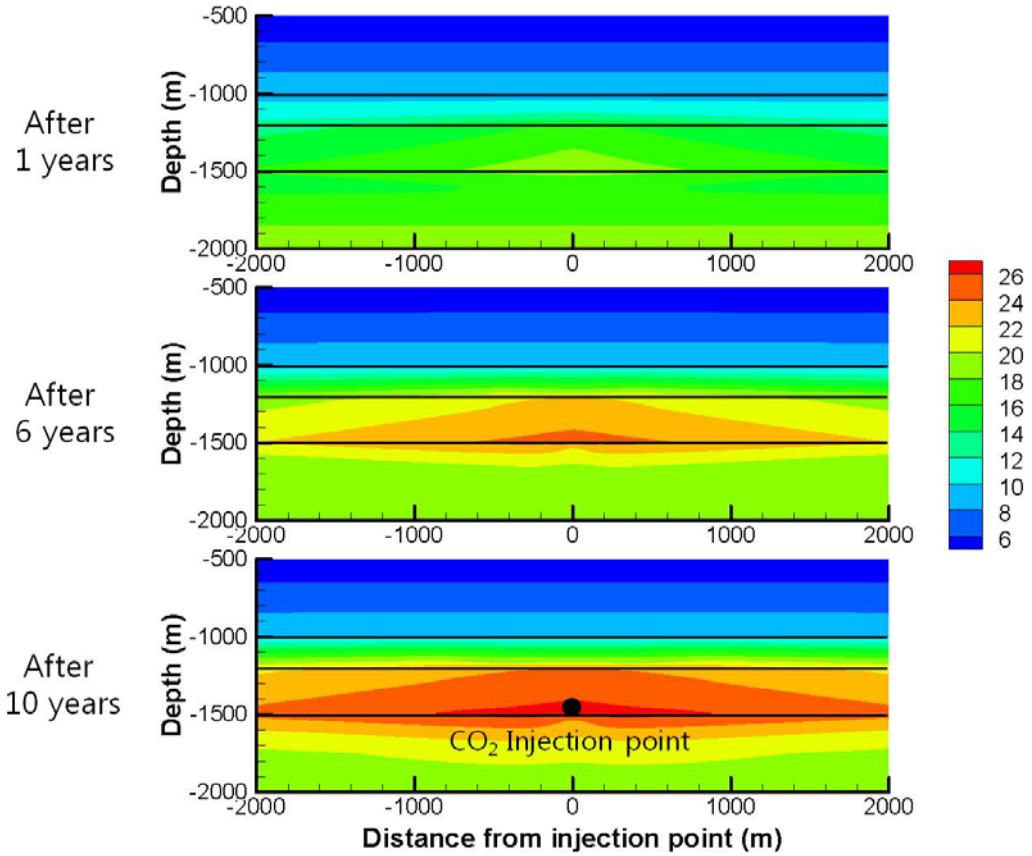

Fig. 12. Pressure change with time near the injection point (Units: MPa)

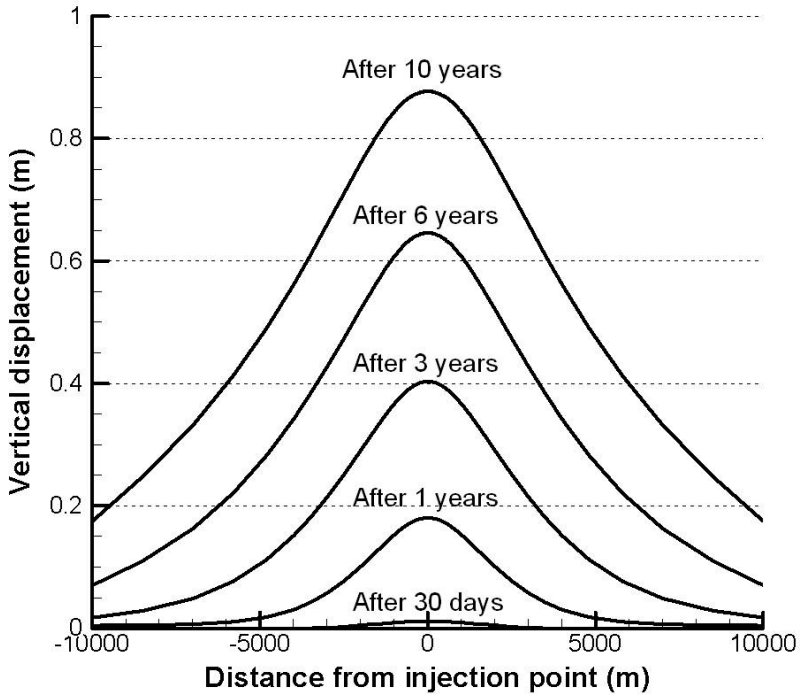

Fig. 13. Vertical displacement of the surface after CO_2 injection

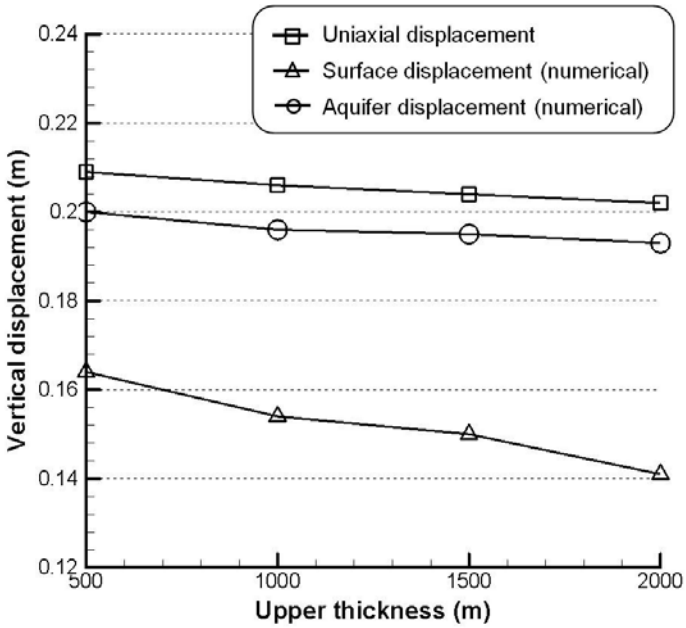

Fig. 14. Vertical displacements of the uniaxial model and the numerical model with reservoir thickness of 100 m

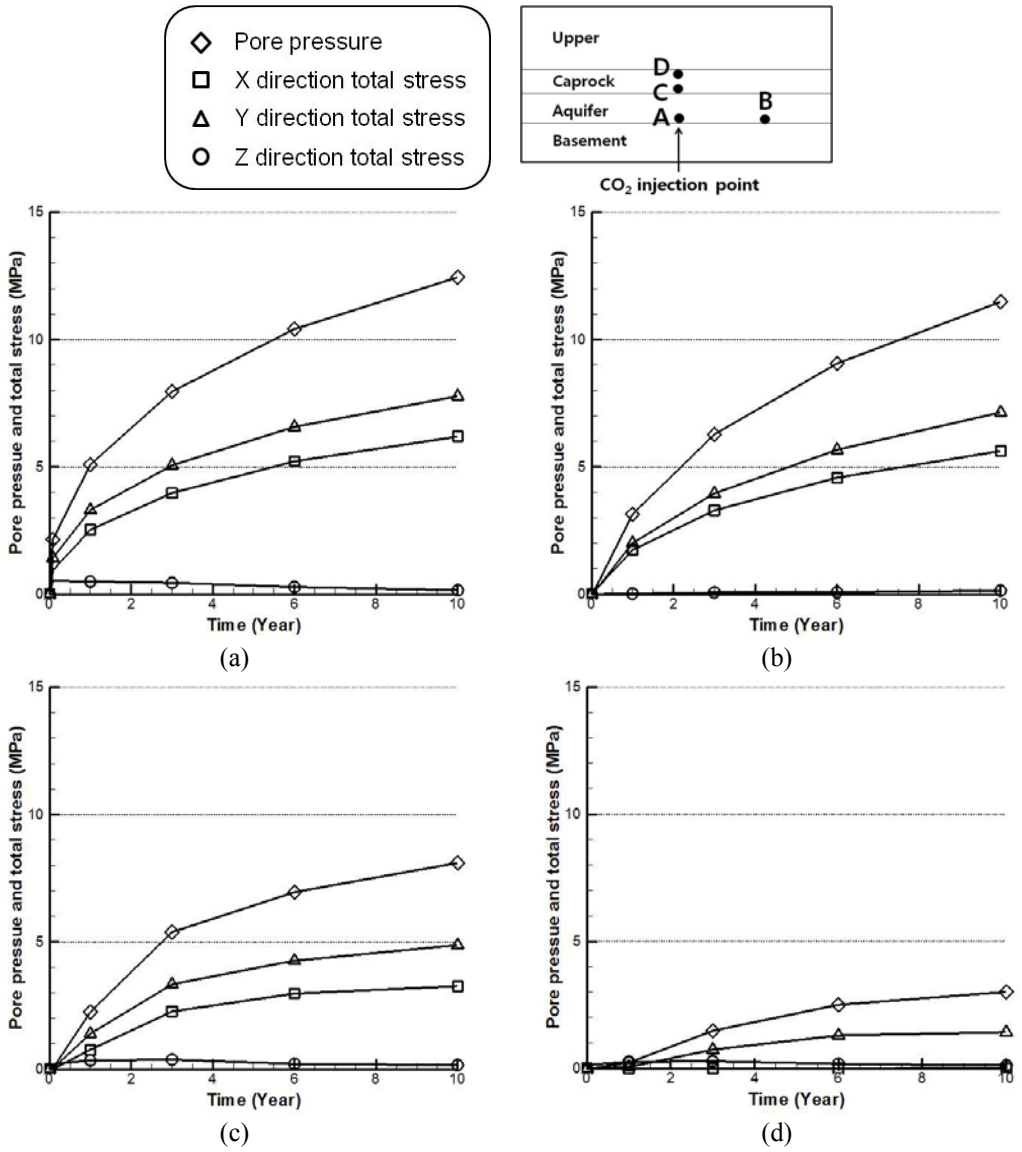

Fig. 15. Increments of pore pressure and total stress: (a) at point A, (b) at point B, (c) at point C, (d) at point D

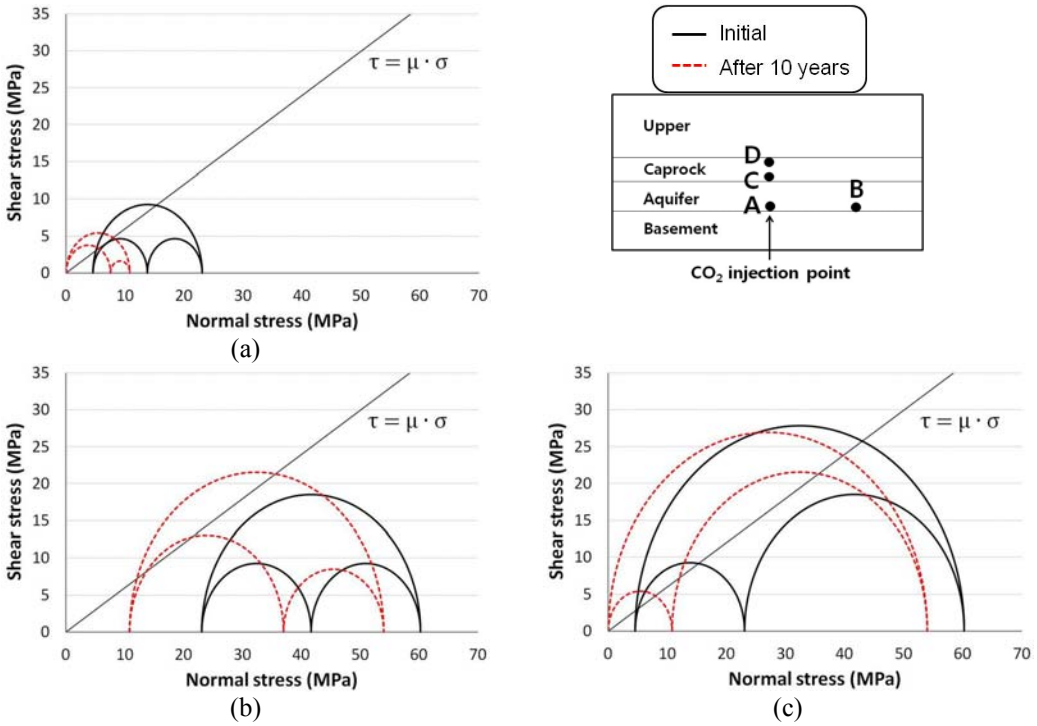

Fig. 16. Mohr circles at point A: (a) normal faulting stress regime, (b) reverse faulting stress regime, (c) strike-slip faulting stress regime

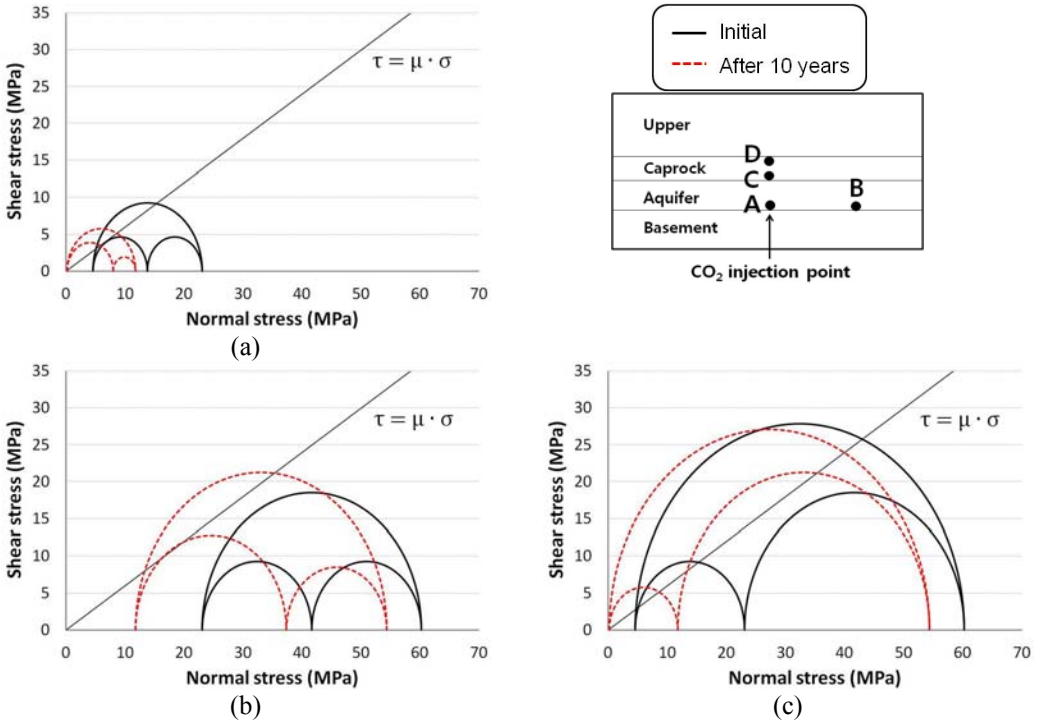

Fig. 17. Mohr circles at point B: (a) normal faulting stress regime, (b) reverse faulting stress regime, (c) strike-slip faulting stress regime

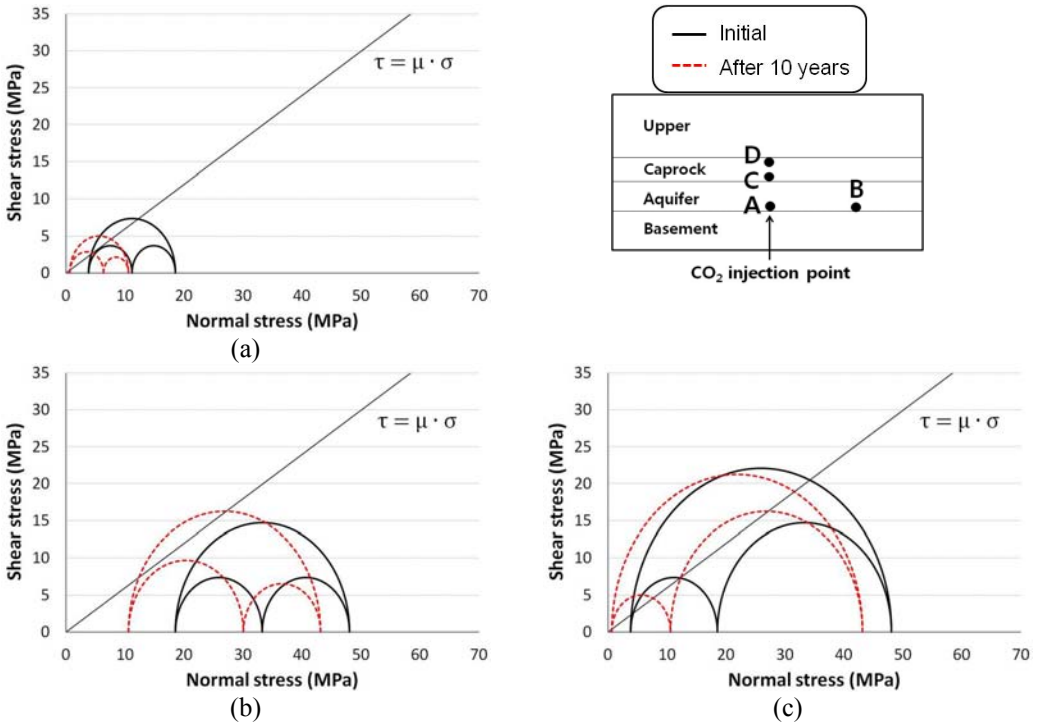

Fig. 18. Mohr circles at point C: (a) normal faulting stress regime, (b) reverse faulting stress regime, (c) strike-slip faulting stress regime

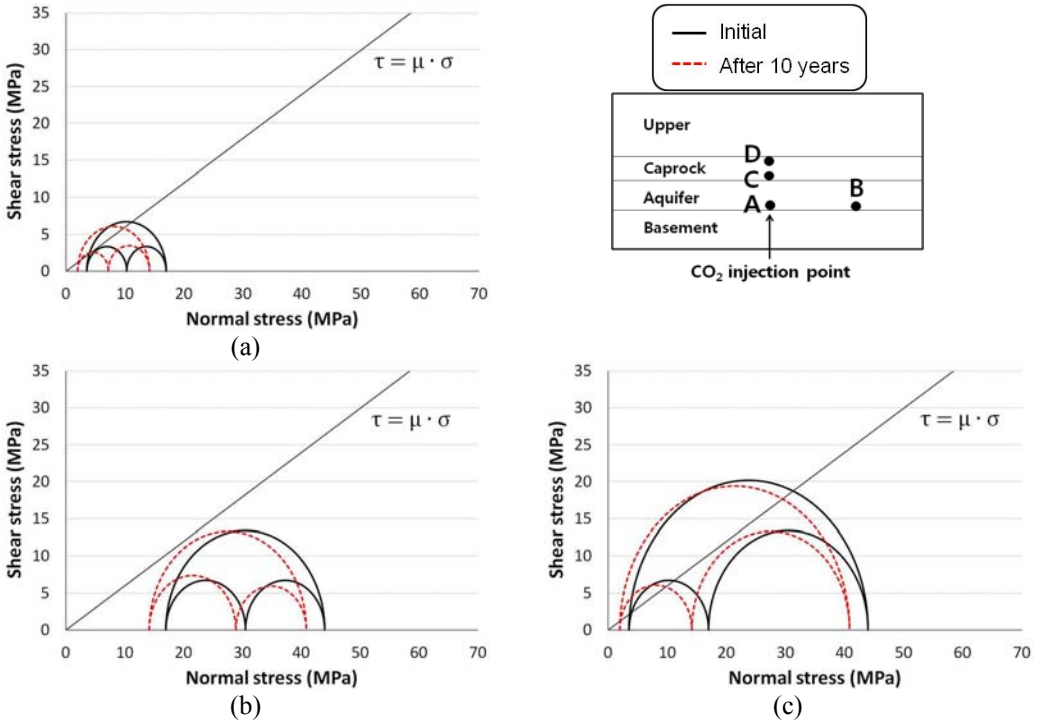

Fig. 19. Mohr circles at point D: (a) normal faulting stress regime, (b) reverse faulting stress regime, (c) strike-slip faulting stress regime

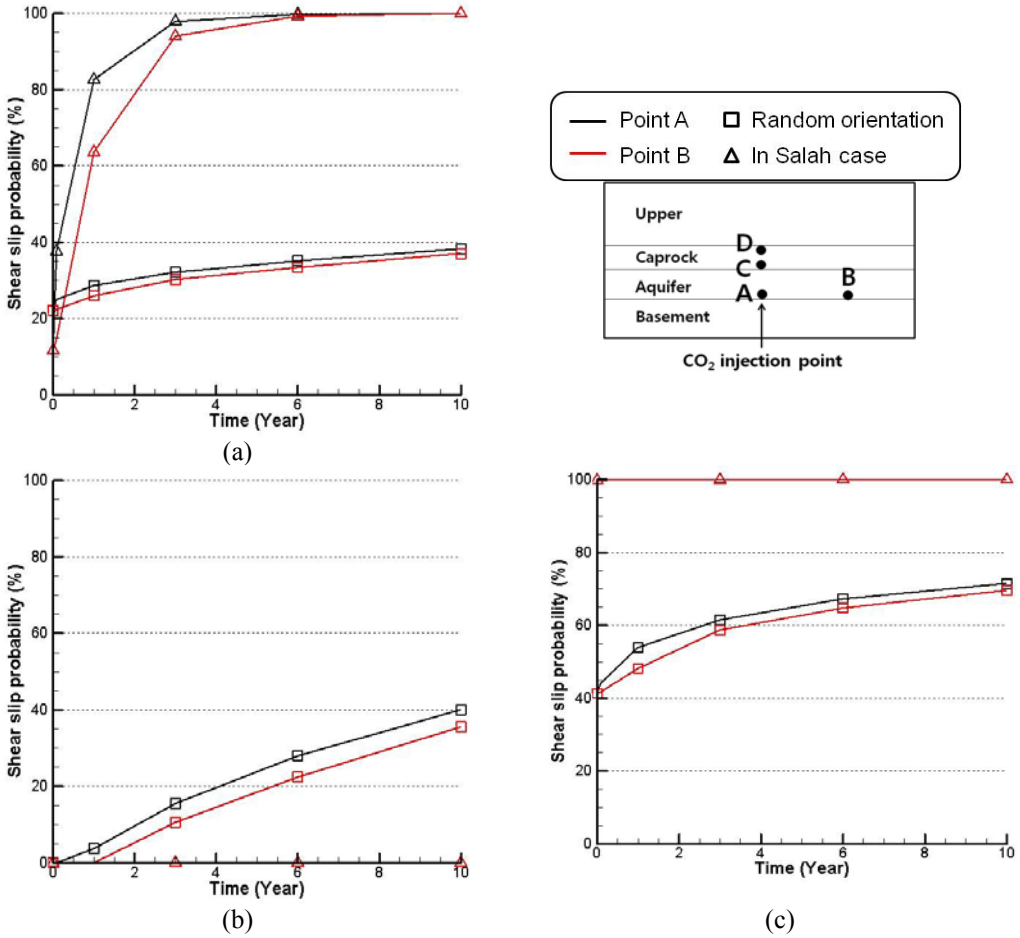

Fig. 20. Evolution of the probability of fracture shear slip at point A and B: (a) normal faulting stress regime, (b) reverse faulting stress regime, (c) strike-slip faulting stress regime

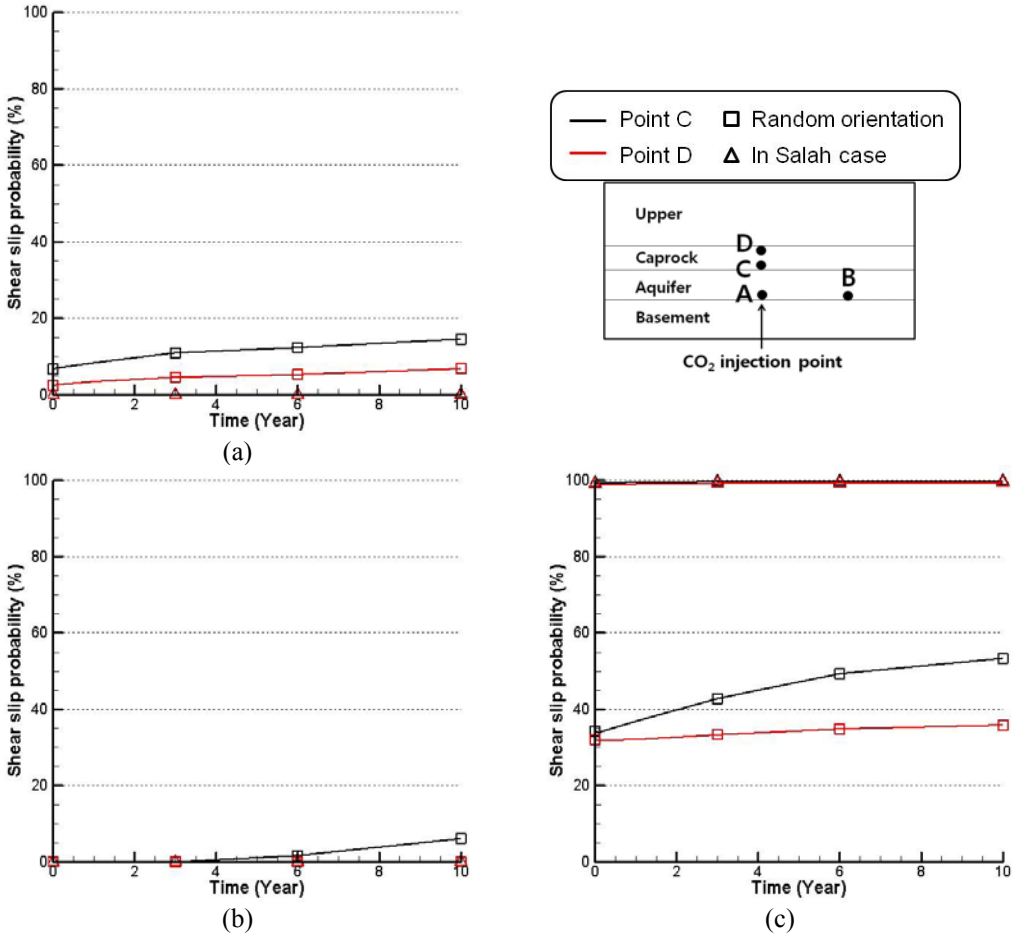

Fig. 21. Evolution of the probability of fracture shear slip at point C and D: (a) normal faulting stress regime, (b) reverse faulting stress regime, (c) strike-slip faulting stress regime

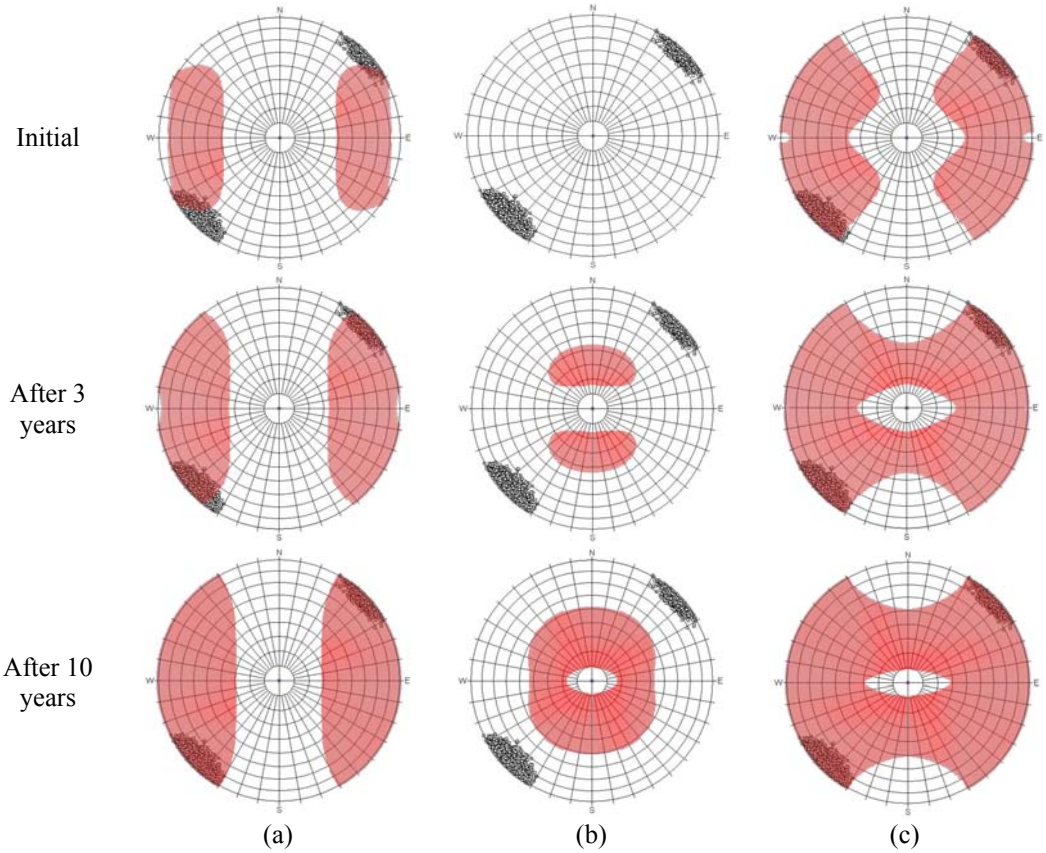

Fig. 22. Shear slip area at point A: (a) normal faulting stress regime, (b) reverse faulting stress regime, (c) strike-slip faulting stress regime

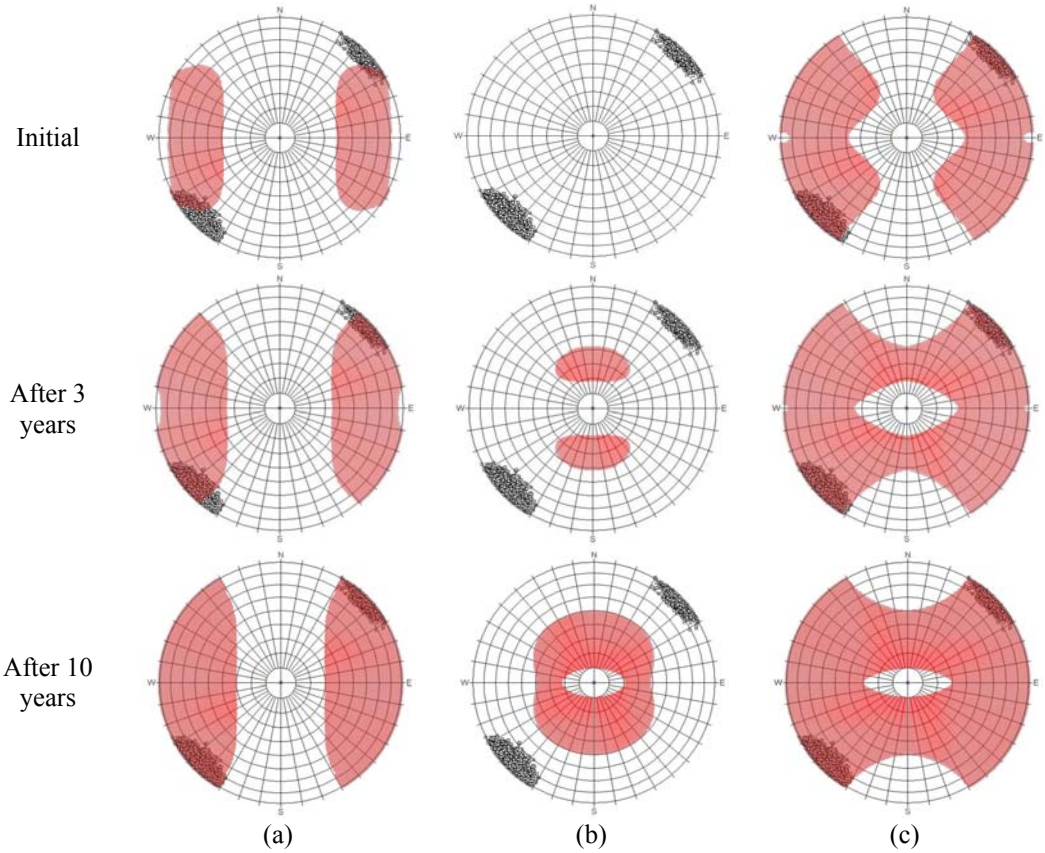

Fig. 23. Shear slip area at point B: (a) normal faulting stress regime, (b) reverse faulting stress regime, (c) strike-slip faulting stress regime

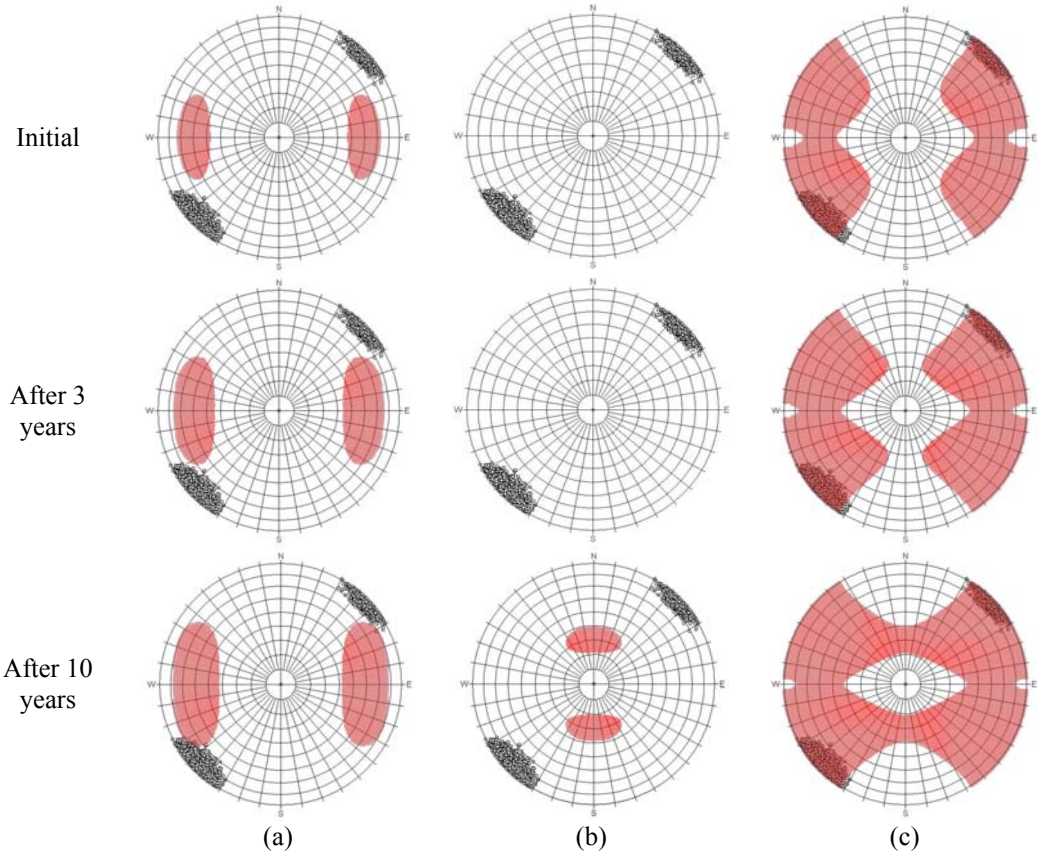

Fig. 24. Shear slip area at point C: (a) normal faulting stress regime, (b) reverse faulting stress regime, (c) strike-slip faulting stress regime

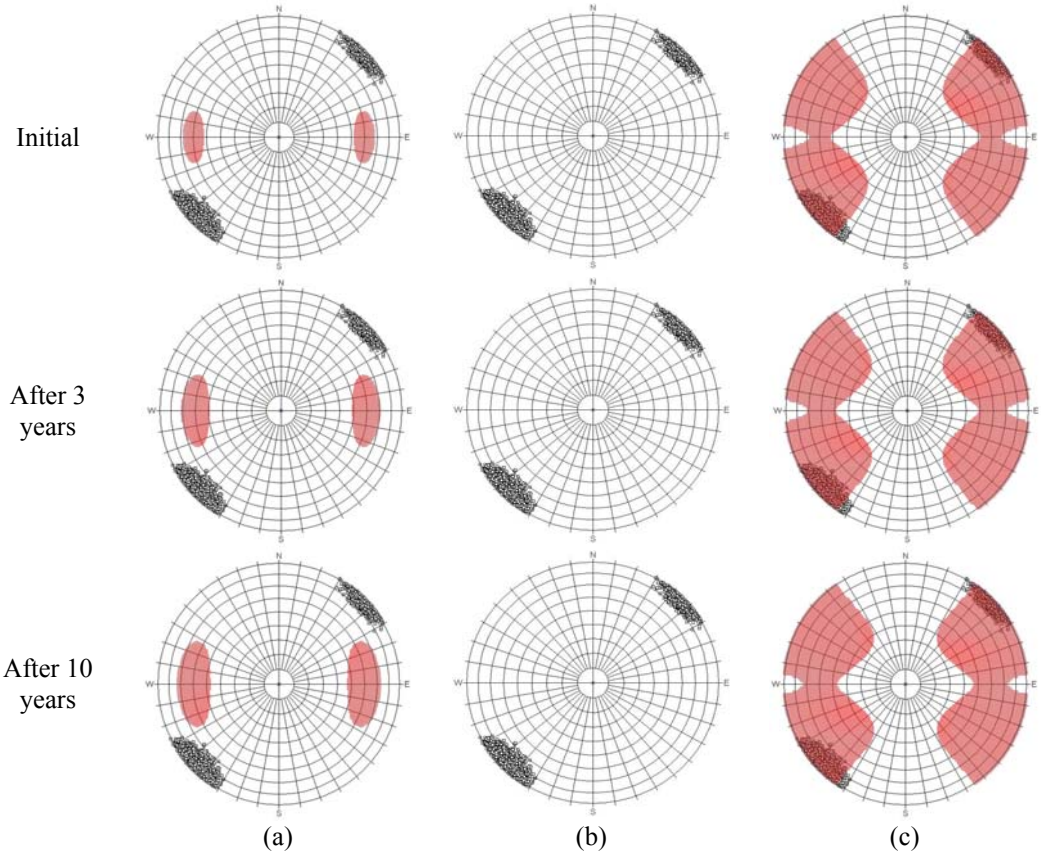

Fig. 25. Shear slip area at point D: (a) normal faulting stress regime, (b) reverse faulting stress regime, (c) strike-slip faulting stress regime

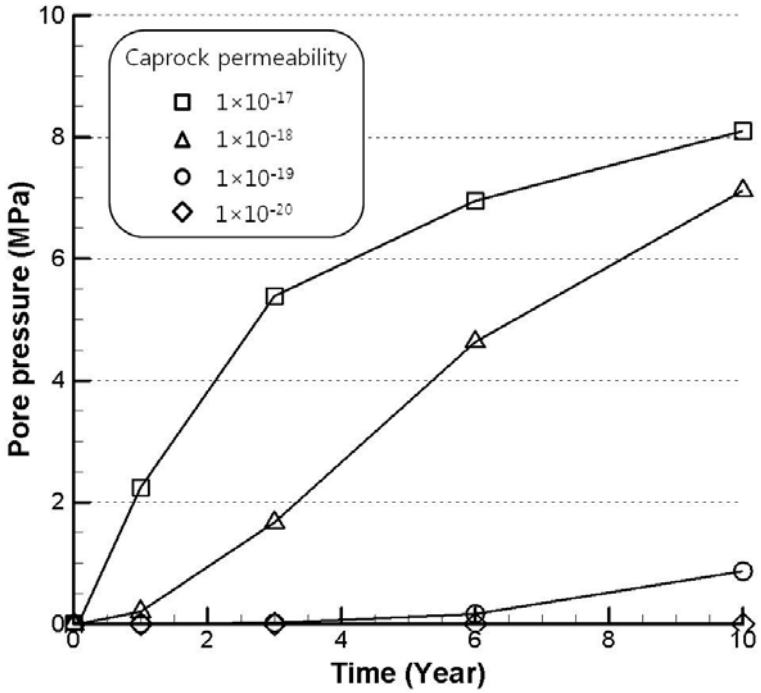

Fig. 26. Pore pressure evolution at point C with different caprock permeability

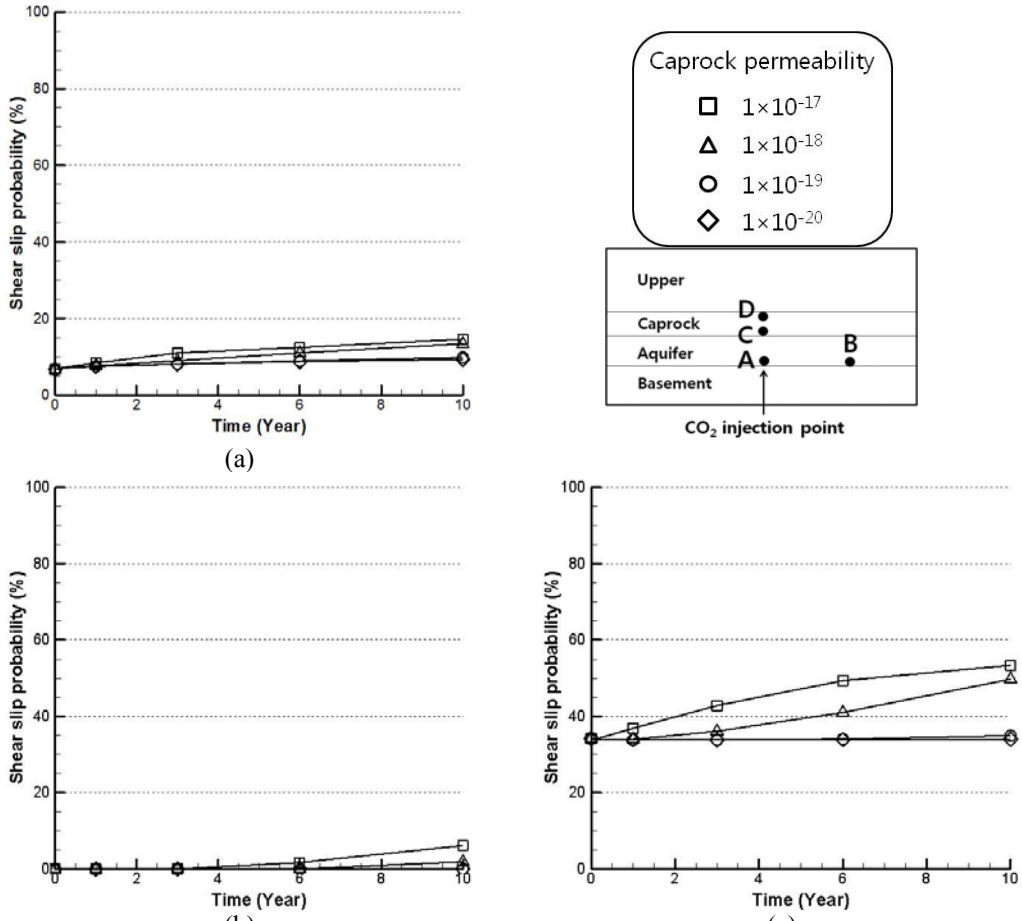

Fig. 27. Probability of fracture shear slip at point C with random fracture orientations for different caprock permeability: (a) normal faulting stress regime, (b) reverse faulting stress regime, (c) strike-slip faulting stress regime